

01 Aug 1994

Asymmetric Upwarp of the Asthenosphere beneath the Baikal Rift Zone, Siberia

Stephen S. Gao
Missouri University of Science and Technology, sgao@mst.edu

Paul M. Davis

Kelly H. Liu
Missouri University of Science and Technology, liukh@mst.edu

Philip D. Slack

et. al. For a complete list of authors, see https://scholarsmine.mst.edu/geosci_geo_peteng_facwork/95

Follow this and additional works at: https://scholarsmine.mst.edu/geosci_geo_peteng_facwork



Part of the [Geology Commons](#)

Recommended Citation

S. S. Gao et al., "Asymmetric Upwarp of the Asthenosphere beneath the Baikal Rift Zone, Siberia," *Journal of Geophysical Research*, vol. 99, no. B8, pp. 15319-15330, American Geophysical Union (AGU), Aug 1994. The definitive version is available at <https://doi.org/10.1029/94JB00808>

This Article - Journal is brought to you for free and open access by Scholars' Mine. It has been accepted for inclusion in Geosciences and Geological and Petroleum Engineering Faculty Research & Creative Works by an authorized administrator of Scholars' Mine. This work is protected by U. S. Copyright Law. Unauthorized use including reproduction for redistribution requires the permission of the copyright holder. For more information, please contact scholarsmine@mst.edu.

Asymmetric upwarp of the asthenosphere beneath the Baikal rift zone, Siberia

S. Gao,¹ P. M. Davis,¹ H. Liu,¹ P. D. Slack,¹ Y. A. Zorin,² N. A. Logatchev,² M. Kogan,³ P. D. Burkholder,⁴ and R. P. Meyer⁴

Abstract. In the summer of 1991 we installed 27 seismic stations about lake Baikal, Siberia, aimed at obtaining accurately timed digital seismic data to investigate the deep structure and geodynamics of the Baikal rift zone and adjacent regions. Sixty-six teleseismic events with high signal-to-noise ratio were recorded. Travel time and Q analysis of teleseisms characterize an upwarp of the lithosphere-asthenosphere boundary under Baikal. Theoretical arrival times were calculated by using the International Association of Seismology and Physics of the Earth's interior 1991 Earth model, and travel time residuals were found by subtracting computed arrival times from observed ones. A three-dimensional downward projection inversion method is used to invert the P wave velocity structure with constraints from deep seismic sounding data. Our results suggest that (1) the lithosphere-asthenosphere transition upwarps beneath the rift zone, (2) the upwarp has an asymmetric shape, (3) the velocity contrast is -4.9% in the asthenosphere, (4) the density contrast is -0.6% , and (5) the P wave attenuation contrast t^* is 0.1 s.

Introduction

The deepest lakes in the world occur in continental rift zones. The deepest of all, Lake Baikal, which contains 20% of the world's fresh water, is in the Baikal rift zone located in East Siberia. The second deepest lake is Tanganyika, within the East African rift system. The Baikal rift zone separates the Siberian craton to the north and northwest from the Sayan-Baikal fold belt to the south and southeast. Here we report results from a seismic array study in this region, designed to probe the mantle beneath lake Baikal and compare this rift with the East African rift [Dahlheim *et al.*, 1989; Davis, 1991; Halderman and Davis, 1991; Green *et al.*, 1991], the Rio Grande rift [Davis *et al.*, 1984; Parker *et al.*, 1984; Davis, 1991], and the Rhine graben [Glahn and Granet, 1992].

Plate tectonics has provided a framework for understanding oceanic geology. However, continental geology

has proved to be enigmatic. In the plate tectonic scheme the continents are undeformable blocks making up part of the interiors of plates. Plates grow at mid-ocean ridges and shrink as they are consumed at subduction zones. The relative immobility of hotspot traces has led to the view that plates slide horizontally over a passive, effectively stationary asthenosphere. However, the continents are not undeformable blocks. They extend at rift zones, such as the basin and range province of North America, and shorten in mountain regions such as the Tibet and Tianshan systems. Nor is the asthenosphere stationary and passive. Hotspot traces give evidence of vertical flow in the asthenosphere which breaks through the lithosphere. An upward flow in the asthenosphere beneath Lake Baikal has been proposed as responsible for the rifting. Our experiment was designed to examine this possibility. We find that the lithosphere-asthenosphere transition upwarps beneath the rift zone, similar to our results from the Gregory rift of the East African rift system.

The Baikal rift zone of Siberia lies along the junction of the stable Siberian craton and the Sayan-Baikal mobile fold belt. The 1500 km en echelon system of rift depressions is the most seismically active continental rift in the world [Golenetsky and Misharina, 1978; Golenetsky, 1990]. During the past 270 years, 13 earthquakes with magnitude larger than 6.5 have occurred within the area [Doser, 1991]. As well as containing water over 1620 m deep, the graben forming the lake is filled with sediments up to 6 km deep [Zorin, 1971; Logatchev and Florensov, 1978]. It is a region of high heat flow: 75–120 mW/m² compared to 38–42 mW/m² on the Siberian platform and 40–60 mW/m² on the fold belts [Lubimova, 1969; Morgan, 1982; Lysak, 1984]. Magne-

¹Department of Earth and Space Sciences, University of California, Los Angeles.

²Institute of the Earth's Crust, Siberian Branch of Russian Academy of Sciences, Irkutsk, Russia.

³Institute of Physics of the Earth, Russian Academy of Sciences, Moscow, Russia.

⁴Department of Geology and Geophysics, University of Wisconsin, Madison.

totelluric studies delineate a zone of high electrical conductivity in the depth range 75-90 km beneath the rift and 180-200 km beneath the adjacent regions [Gornostaiev et al., 1970; Popov, 1990].

Estimates of total horizontal extension across the rift range from 10 km [Logatchev and Florensov, 1978] to 20 km [Zorin and Cordell, 1991]. Gravity anomalies and deep seismic soundings (DSS) reveal that crustal thickness increases from 34-35 km beneath the rift axis to 42-46 km beneath the adjacent margins [Zorin et al., 1989]. Compressional wave velocity in the crust is 6.4 km/s, based upon deep seismic soundings. In the upper mantle it is 7.7 km/s beneath the rift zone but 8.1-8.2 km/s beneath the adjacent platform [Puzryev et al., 1978].

There are indications from seismic, gravity, and magnetotelluric studies that the asthenosphere upwarps beneath the Baikal rift, relative to adjacent regions. However, the size and shape of this upwarp are not well known. Some argue that the peak of the asthenospheric diapir reaches the Moho, that is, that the lithosphere is

thinned to the thickness of the crust, while others believe it is much deeper [Logatchev and Zorin, 1987; Zammarayev and Ruzhich, 1978; Zorin et al., 1989; Popov, 1990]. The purpose of this study is to use accurately timed teleseismic signals to investigate the velocity contrast and geometry of the lithosphere-asthenosphere boundary beneath the area.

The teleseismic P wave method for investigating crustal and upper mantle structure has been employed widely in continental rift zones [Davis, 1991; Davis et al., 1984; Parker et al., 1984; Dahlheim et al., 1989; Halderman and Davis, 1991; Green et al., 1991; Glahn and Granet, 1992]. The method consists of timing P wave arrivals from distant earthquakes and comparing observed arrival times with those expected for a laterally homogeneous Earth model. The residuals are then explained in terms of local three-dimensional heterogeneity in the velocity field. Given enough angles of incidence and azimuths of incoming rays to the observational network, the residual pattern can be used in a linearized inversion to determine velocity variations. The teleseismic

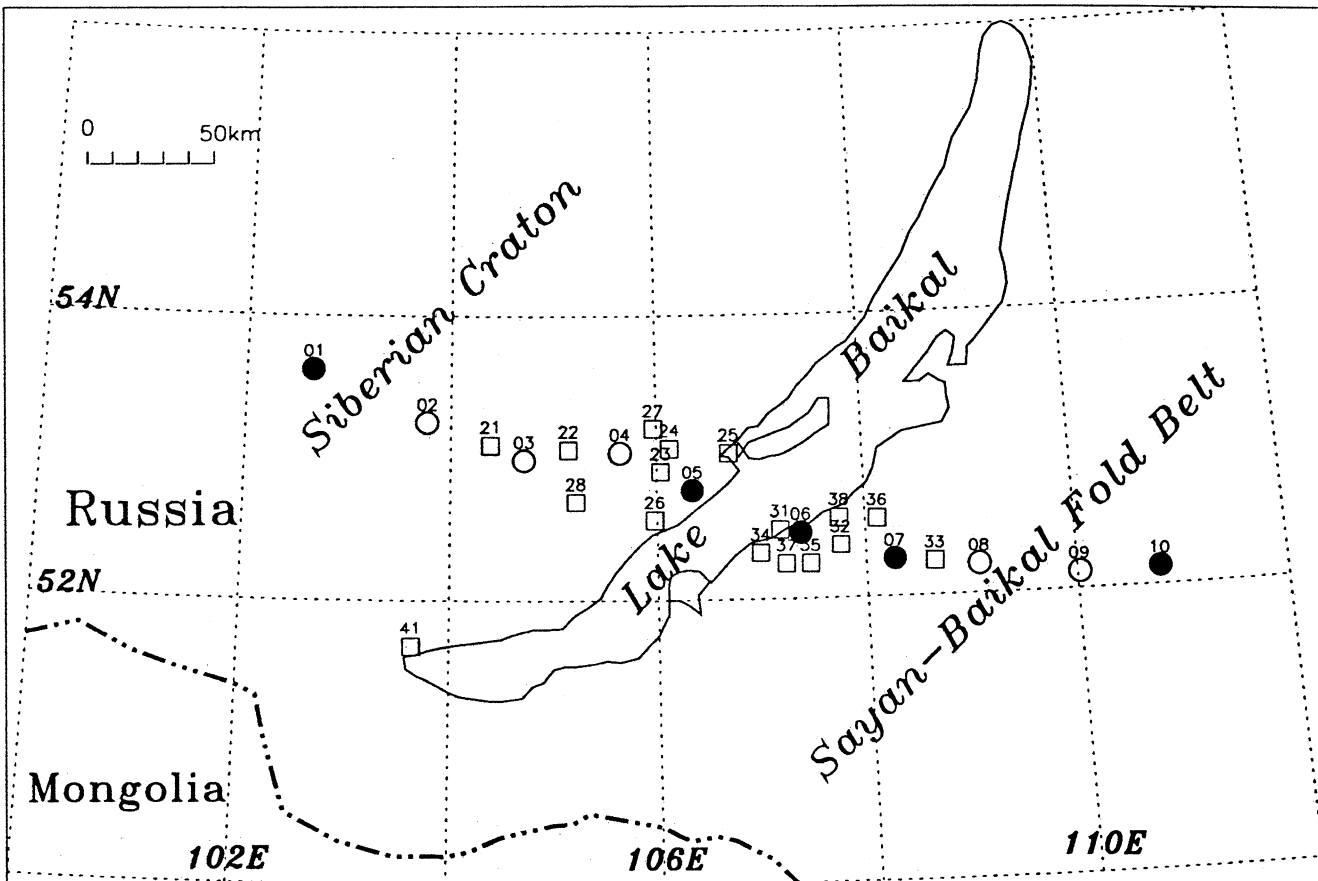


Figure 1. Map showing station locations of the University of California, Los Angeles (UCLA), University of Wisconsin, Madison (UW), and Russian Academy of Sciences Baikal 1991 Seismic Array Study Project. All 27 stations were equipped with 1-Hz three-dimensional sensors and five of the stations were cosited with broadband sensors (four Guralp CMG-3V vertical sensors and one STS2 three-component sensor). The network ran from early July to early October, 1991. Sixty-six teleseismic events with high signal-to-noise ratio were recorded. Circles are UCLA Reftek stations among which the solid circles were cosited with broadband sensors; squares are UW stations.

Table 1. The 1991 Baikal Rift Project Station Information

Station	Coordinates		Elevation, m	Sensor
	Latitude, °N	Longitude, °E		
01	53.620	102.645	550	L4C, Guralp
02	53.246	103.767	468	L4C
03	52.984	104.714	610	L4C
04	53.034	105.648	820	L4C
05	52.767	106.345	910	L4C, Guralp
06	52.464	107.379	871	L4C, STS2
07	52.264	108.273	830	L4C, Guralp
08	52.207	109.078	810	L4C
09	52.118	110.024	772	L4C
10	52.172	110.785	994	L4C, Guralp
21	53.089	104.386	634	HS10
22	53.058	105.146	751	HS10
23	52.900	106.040	761	HS10
24	53.062	106.128	784	HS10
25*	53.025	106.701	619	HS10
26	52.559	105.977	886	HS10
27	53.203	105.973	693	HS10
28	52.690	105.217	560	HS10
31*	52.537	107.180	580	HS10
32*	52.370	107.759	632	HS10
33*	52.241	108.654	645	HS10
34	52.325	106.986	762	HS10
35	52.245	107.463	718	HS10
36	52.549	108.120	543	HS10
37	52.246	107.231	644	HS10
38	52.559	107.751	850	HS10
41*	51.680	103.644	560	HS10

* Stations not used in this study.

method is probably the most effective approach to investigate heterogeneous structure of the upper mantle.

Data and Method

In the summer of 1991, we installed 27 seismic stations about Lake Baikal (10 Program for Array Seismic Studies of the Continental Lithosphere Reftek recorders and 17 University of Wisconsin, Madison, recorders) (Figure 1 and Table 1). The array was quasi-linear, with limited breadth near the lake. All the stations were equipped with 1-Hz 3-component sensors and five of the stations were cosited with broadband seismometers. The digital seismographs synchronize internal clocks to signals from the Omega navigation system, which ensured that the timing error for most of the data was less than 20 ms. Figure 2 shows a record section of a northern California event on vertical sensors.

The network ran from early July to early October 1991. Seismograms from 66 events with sufficient signal-to-noise ratio to be used in an inversion were recorded. Theoretical arrival times were calculated by using the International Association of Seismology and Physics of the earth's Interior (IASPEI) 1991 Earth model [Kennett and Engdahl, 1991]. Residuals were found by subtracting these theoretical arrival times from observed ones, and relative residuals were formed for each event by subtracting the event's mean residual from the raw residuals (Figure 3). Examples are shown in Figure 3, where events are separated into clusters having similar azimuths and epicentral angles. The relative residual curves within these groups of events have similar variation patterns. The strong dependence of relative residuals upon hypocentral location suggests that the main velocity interface responsible for this variation, that is,

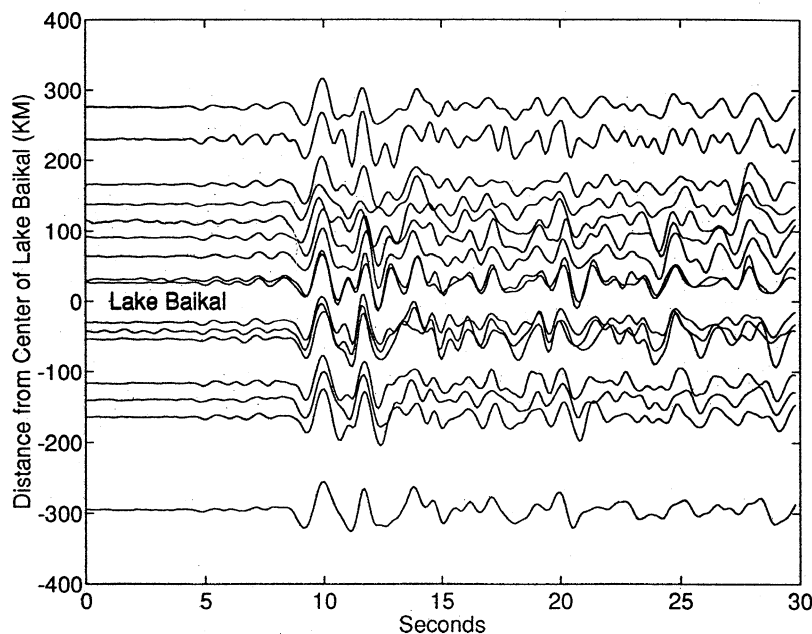


Figure 2. Sample seismograms recorded by the vertical components. Event time: day 229, 1992 2217 UT; location: 41.606°N, 125.506°W; mb, 6.2; depth, 10 km. Positive direction is to the east.

the lithosphere-asthenosphere boundary, varies three-dimensionally within the studied area.

We use a simple three-dimensional downward projection method developed from a previous two-dimensional procedure [Davis *et al.*, 1984; Halderman and Davis, 1991; Davis, 1991] to estimate the configuration of the velocity interface. The method assumes straight rays and a plane wave approximation. Travel time residuals T_{ij} at the i th station from the j th earthquake are calculated by removing the mean and are rotated to obtain T'_{ij} , which are values which would have been obtained for vertical incidence if the surface varies slowly and no other structural complications are present, that is,

$$T'_{ij} = T_{ij} \cos I_{ij} \quad (1)$$

where I_{ij} is the angle of incidence of the rays from the j th earthquake at the i th station. The coordinates

of the i th station (X_i, Y_i) are transformed to values (X'_{ij}, Y'_{ij}) projected along the ray path, that is, the coordinates of the intercept points of the rays and the asthenosphere upper boundary,

$$X'_{ij} = X_i + D \tan I_{ij} \sin(\theta_{ij} - \phi) - A \sin(I_{ij}) T_{ij} \operatorname{sgn}[\sin(\theta_{ij} - \phi)] \quad (2)$$

$$Y'_{ij} = Y_i + D \tan I_{ij} \cos(\theta_{ij} - \phi) - A \sin(I_{ij}) T_{ij} \operatorname{sgn}[\cos(\theta_{ij} - \phi)] \quad (3)$$

where $A = V_1 V_2 / (V_1 - V_2)$, and V_1 and V_2 are the velocities above and below the boundary, respectively; $\operatorname{sgn}(x) = \pm 1$, depending on the sign of x ; θ_{ij} is the azimuth from the j th event to the i th station; ϕ is the orientation of the $+y$ direction clockwise from the north and D is the mean depth of the interface.

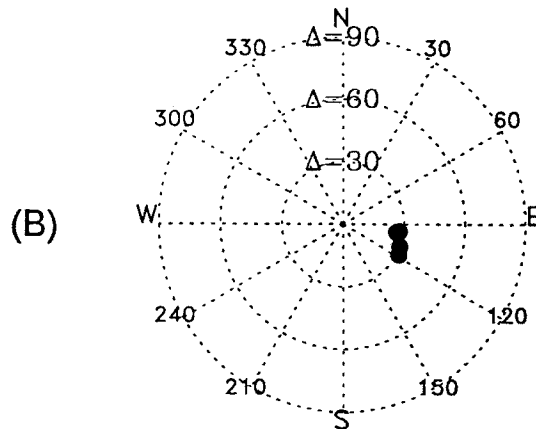
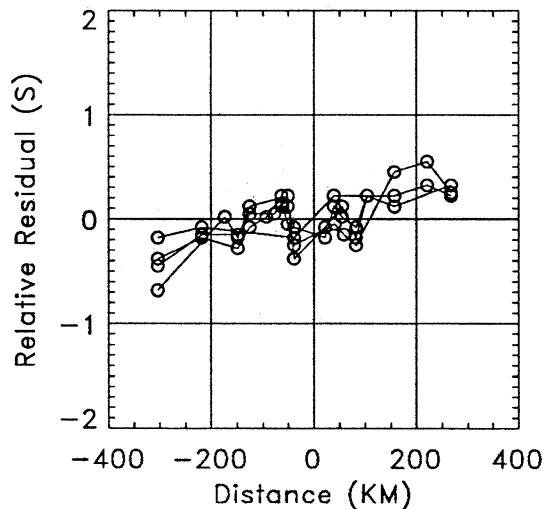
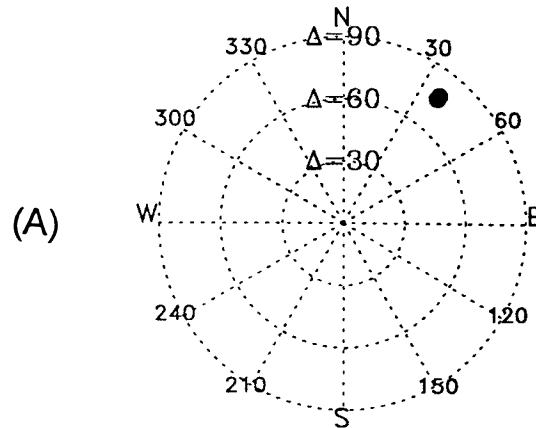
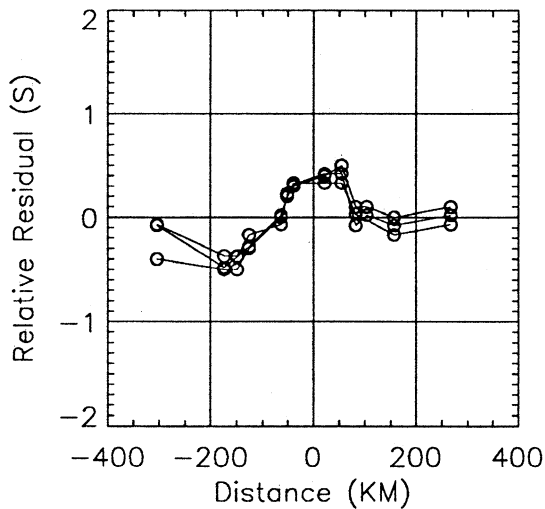


Figure 3. Teleseismic travel time delays relative to International Association of Seismology and Physics of the Earth's Interior 1991 Earth model. Events are separated into clusters having similar azimuths and epicentral angles (right diagrams). Center of the polar map is the center of the array. Relative residual curves within these event clusters have similar patterns. Delay patterns show strong dependence on hypocentral locations (left diagrams). Zero distance corresponds to the center of Lake Baikal along the profile.

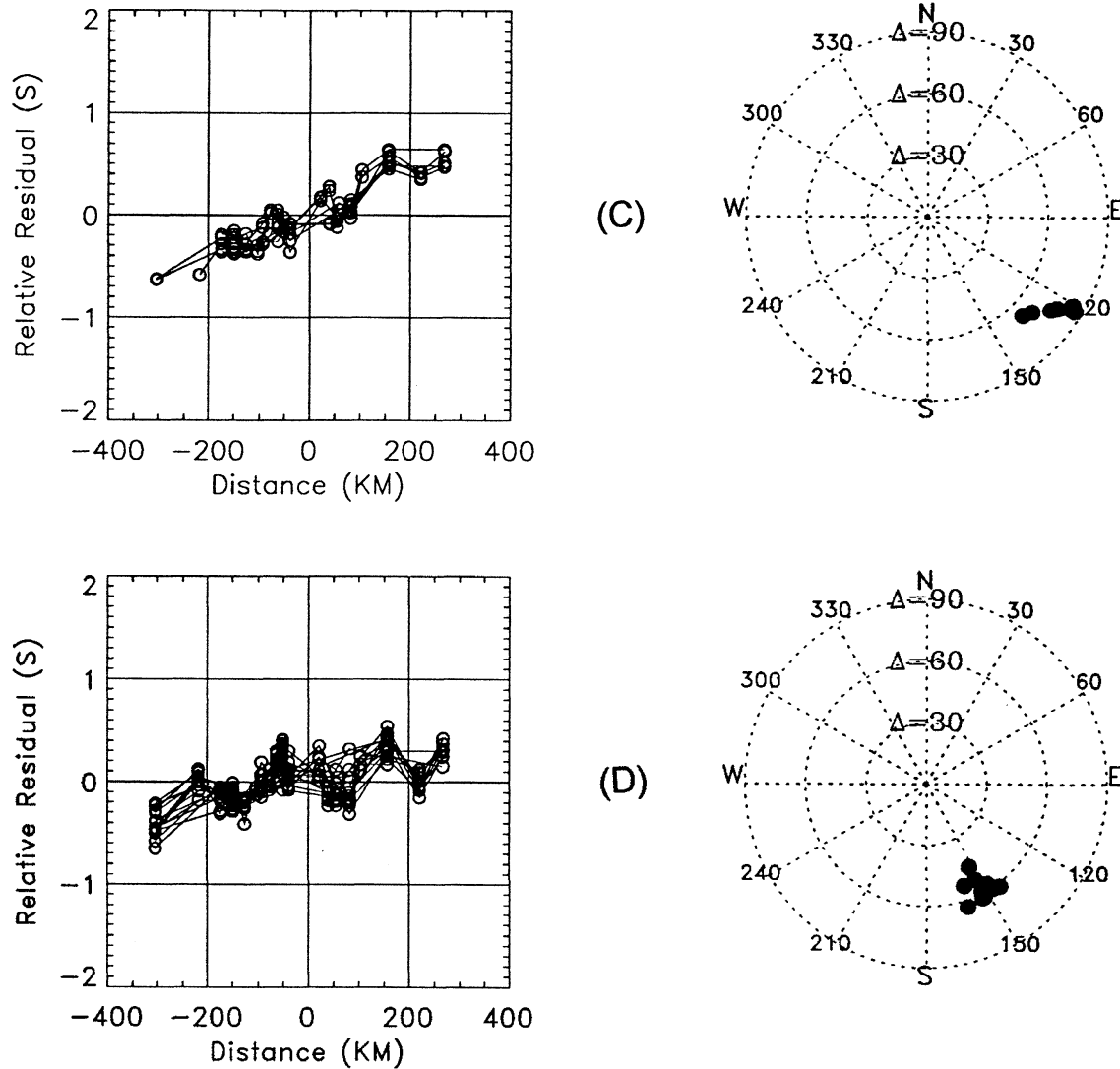


Figure 3. (continued)

Values are found for D and A by minimizing the misfit of the T'_{ij} to an n th order polynomial in both the X'_{ij} and Y'_{ij} . To compensate for any bias introduced in the array mean if different numbers of stations are used for different earthquakes, and to take into account the large origin time uncertainty, an offset time for the j th earthquake, ΔT_j , is included in the least squares fit.

The travel time curves of Figure 3 show that all the 6 clusters tilt toward east, indicating lower compressional wave velocity on the eastern side. Events from the east and southeast (Figures 3b, 3c, and 3d, respectively) have significantly greater slopes than events from the northeast, south, and southwest (Figures 3a, 3e, and 3f, respectively). This is particularly noticeable in Figure 3c. We consider 3 possible causes for the differences in the slopes. The first interpretation is that a low velocity structure is present beneath the southeast flank of the lake. When we examine the ray paths, taking into account that the rays have small angles of incidence (about 20°) and therefore sample nearly the same volume beneath the array, we find that the struc-

ture must be narrow, deep, and dike-like with strike of 130° . If this is the cause, it cannot be resolved uniquely by the aperture of our array. Secondly, it is possible these different slopes are due to systematic mislocation of events, especially those that occurred in the trenches (in regions of Figures 3b, 3c, and 3d). The near-source stations used to locate them were almost all at one side of the event, and hence a systematic mislocation is very plausible [Dziewonski and Anderson, 1981]. The error in the position and the origin time must be compensated by an equivalent error in depth, which leads to the tilt of a derived travel time curve [Dziewonski and Anderson, 1981]. We calculated that for an earthquake of intermediate focal depth, at 40° from the center of the array, a 50-km depth mislocation causes a slope error in the travel time residual curves of 0.3 ms/km, that is, a 0.17-s variation along a profile of 550 km such as ours. Many of the events from this region are assigned a nominal depth of 33 km in the catalog (Table 2), implying that depth resolution is highly uncertain. The third possible cause is the inaccuracy of the standard

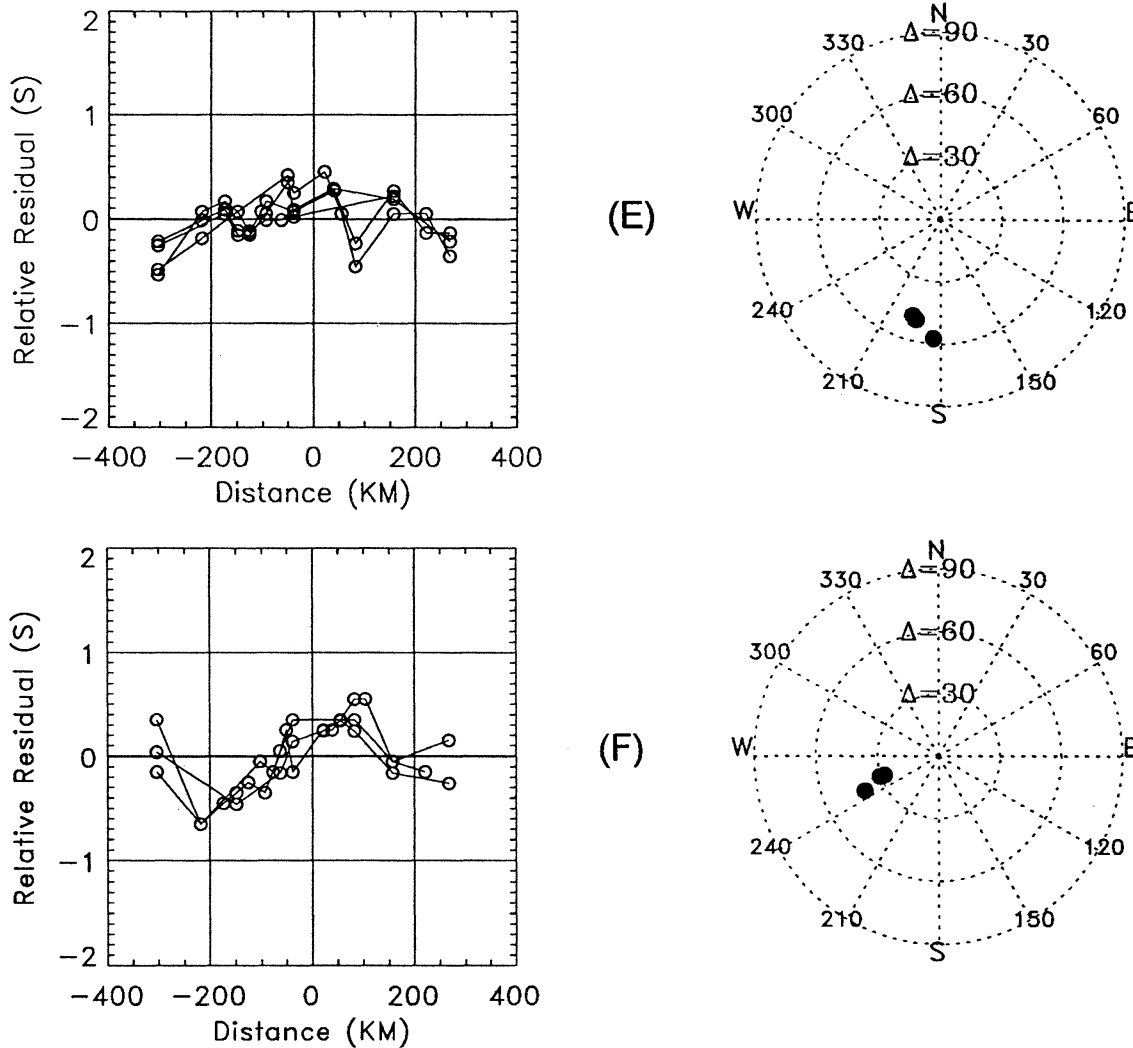


Figure 3. (continued)

Earth model. The Banda Sea and adjacent regions lie in one of the extremes in lateral heterogeneity in the upper mantle, owing to the large amount of subduction that occurs there. Thus a laterally homogeneous Earth model such as IASPEI 91 may not give the correct travel times for those events.

In order to take into account for anomalous travel time slopes, either from velocity heterogeneity outside the volume directly beneath our array or from event mislocation, we included in our inversion two constrained slope terms S_{xj} and S_{yj} . The result of the inversion (see next sections) suggests that the different travel time slopes can be reconciled if most of the events in the 3 trench groups (Figures 3b, 3c, and 3d) had been located about 40 km too shallow.

A Priori Constraints on the Inversion

The three-dimensional downward projected residual T'_{ij} is given by

$$T'_{ij} = \Delta T_j + \sum_{k=0}^n \sum_{l=0}^{n-k} a_{lk} X_{ij}^{lk} Y_{ij}^{ll} + S_{xj} X'_{ij} + S_{yj} Y'_{ij} \pm \sigma_{ij} \quad (4)$$

with the constraints

$$\Delta T_j = 0.0 \pm \sigma_{ej} \quad (5)$$

$$S_{xj} = 0.0 \pm \sigma_{s1j} \quad (6)$$

$$S_{yj} = 0.0 \pm \sigma_{s2j} \quad (7)$$

$$a_{00} = D = D_0 \pm \sigma_D \quad (8)$$

$$A = A_0 \pm \sigma_A \quad (9)$$

where σ_{ij} , σ_{ej} , σ_{s1j} , σ_{s2j} , σ_D , and σ_A are a priori standard deviations of the residuals, event offsets, slopes in X' and Y' , and depth and velocity factor, respectively; σ_{ij} and σ_{ej} are taken as 0.1 s; σ_{s1j} and σ_{s2j} are chosen as 0.05 ms/km and 0.15 ms/km, respectively; and D_0 and A_0 are a priori estimates of the depth and velocity factor. The standard deviations act as damping factors for the variables. A larger standard deviation results in smaller damping and hence allows larger changes in the inversion from the initial estimates. More information on constrained inversion can be found in the work by Jackson and Matsu'ura [1985].

On their own, the teleseismic residuals permit a wide range of lithosphere-asthenosphere boundaries that

Table 2. Events Used for the Inversion of Baikal 1991 Data

Group	Geographic Region	Origin		Coordinates		Depth, km	m_b	Offset, ms	X Slope, ms/km	Y Slope, ms/km
		Day	Time, UT	Latitude, °N	Longitude, °E					
A	Northern California	228	2226.17.4	41.729	-125.386	10	5.7	1.96	-0.63	-3.56
A	Northern California	229	1929.40.0	40.235	-124.348	12	6.1	-82.89	-0.31	-4.39
A	Northern California	229	2217.12.8	41.606	-125.506	10	6.2	-13.43	-0.56	-3.92
B	Honshu, Japan	205	0936.37.8	32.257	138.809	249	5.2	5.38	0.16	6.78
B	Honshu, Japan	218	1449.31.3	35.736	141.081	34	5.8	-32.61	-0.24	4.23
B	Hokkaido, Japan	238	1459.46.6	42.025	144.698	45	5.8	-43.96	-0.66	-2.59
B	Hokkaido, Japan	245	0303.42.9	42.292	143.037	66	5.1	-44.40	-0.75	-4.56
B	Honshu, Japan	246	0844.47.9	33.645	138.780	23	5.9	4.76	-0.15	5.47
C	New Britain	220	1526.10.1	-4.672	152.213	175	5.2	-6.17	0.39	7.89
C	Vanuatu	226	1915.06.4	-13.601	167.641	33	6.0	-37.82	0.27	7.30
C	Vanuatu	238	2252.12.4	-14.248	167.813	33	5.1	-3.76	0.41	11.25
C	New Guinea	259	1747.18.4	-5.476	147.012	219	5.0	-20.39	0.19	6.29
C	Vanuatu	259	2219.08.1	-13.263	167.110	165	5.3	-31.82	0.17	8.09
C	Solomon Islands	269	0914.51.5	-9.302	158.609	33	5.2	-37.99	0.30	8.08
C	New Britain	270	2026.56.8	-5.865	151.085	33	5.8	-32.95	0.20	6.34
C	Solomon Islands	275	1432.55.3	-10.421	161.384	93	5.4	2.18	-0.51	3.92
C	Solomon Islands	275	1749.10.2	-10.230	161.053	90	5.3	9.52	-0.61	3.80
D	Halmahera Indonesia	202	2259.10.1	3.011	128.452	40	5.7	4.63	0.05	3.16
D	Mindanao, Philippines	204	1122.10.1	5.817	125.891	146	5.6	6.98	-0.06	2.73
D	Banda Sea	204	2116.31.0	-6.125	130.192	100	5.7	10.55	0.49	5.66
D	Ceram	207	1504.08.9	-2.105	128.043	33	5.2	3.31	0.41	4.41
D	Ceram	210	0150.08.7	-3.027	129.352	33	5.2	7.00	0.05	3.55
D	Leyte, Philippines	214	0627.13.0	10.230	125.178	10	5.0	-0.23	0.07	3.16
D	Minahassa Peninsula	220	0400.01.2	1.267	122.611	45	5.3	-7.14	-0.25	1.57
D	Minahassa Peninsula	220	2208.28.8	1.629	122.947	33	5.0	0.03	0.16	3.77
D	Minahassa Peninsula	221	0628.03.3	1.390	122.701	38	5.4	-8.54	0.00	2.56
D	Ceram	221	2331.56.8	-3.103	129.748	33	5.1	-4.33	0.11	3.91
D	Ceram	223	1443.53.8	-3.182	130.313	33	5.6	7.96	0.07	3.74
D	Ceram	225	2014.14.4	-3.081	130.325	33	5.1	-0.06	0.09	4.00
D	Talaud Island	226	1743.07.5	3.158	127.947	124	5.5	-9.73	0.07	2.95
D	Mindanao, Philippines	235	1616.08.1	9.973	126.116	33	5.2	-12.99	0.34	3.89
D	Timor	235	2016.24.1	-9.220	123.526	29	5.4	-6.73	0.26	4.10
D	Banda Sea	236	1113.09.9	-6.043	130.355	58	5.6	-1.47	0.19	4.11
D	West Irian	242	0129.27.7	-3.349	134.458	33	5.4	12.55	0.02	4.18
D	Irian Jaya	244	0718.30.4	-3.509	134.979	33	5.0	-1.58	0.25	5.15
D	Banda Sea	249	1145.55.2	-6.111	130.578	33	5.1	-9.12	0.15	4.13
D	Irian Jaya	249	1314.49.8	-0.333	132.742	19	5.1	-15.56	0.22	4.52
D	Banda Sea	263	1447.44.9	-6.499	129.871	170	5.4	-16.28	-0.02	3.18
D	Helmahera, Indonesia	266	1548.37.1	2.541	128.420	33	5.0	-6.25	0.25	3.78
D	Banda Sea	267	0506.01.5	-6.533	130.231	70	5.2	-3.96	0.03	4.04
D	Irian Jaya	270	2301.24.6	-3.359	137.562	53	5.5	-5.14	-0.07	3.80
D	Banda Sea	273	1208.48.1	-6.626	130.344	43	5.2	5.26	0.28	5.01
E	Sumatera	204	1325.48.1	3.742	95.962	54	5.8	13.71	0.29	2.43
E	Sumatera	218	0217.32.5	3.801	95.418	25	6.0	2.42	-0.16	1.24
E	Sumatera	237	0501.00.0	5.655	94.116	45	5.2	79.07	0.10	2.71
E	Nicobar Islands	238	2054.24.7	6.889	94.672	33	5.7	0.14	0.13	2.21
F	Pakistan	220	1112.38.9	26.824	65.849	60	5.3	79.39	-0.01	3.31
F	Tajikistan	232	0846.40.5	37.646	72.150	135	5.2	12.03	0.02	2.14
F	Afghanistan	262	0458.36.6	35.921	69.861	99	5.0	-2.39	0.18	2.12
NC*	Southern Alaska	201	1148.47.4	54.553	-161.641	35	5.7	7.56	0.22	-3.45
NC	Kamchatka	205	0310.41.1	52.156	162.256	33	5.1	50.97	-0.61	-1.42
NC	Iran-Iraq	205	0945.42.7	36.501	44.076	33	5.3	6.07	0.27	6.07

Table 2. (continued)

Group	Geographic Region	Origin		Coordinates		Depth, km	m_b	Offset, ms	X Slope, ms/km	Y Slope, ms/km
		Day	Time, UT	Latitude, °N	Longitude, °E					
NC	Mozambique	205	1354.51.6	-18.412	34.690	32	5.1	5.71	0.72	7.44
NC	Leyte, Philippines	214	0627.13.0	10.230	125.178	10	5.0	-0.23	0.07	3.16
NC	Ryukyu Islands	215	0833.16.8	29.330	129.059	16	5.4	-8.10	-0.57	0.16
NC	Aleutian Islands	217	1108.08.9	51.674	176.376	33	5.1	119.46	-0.88	-1.66
NC	Mariana Islands	225	2231.44.8	18.902	145.167	605	5.1	-13.64	0.16	6.33
NC	Aleutian Islands	226	1253.28.3	54.334	-169.343	299	5.7	-23.66	-0.18	-1.94
NC	Volcano Islands	228	0147.47.0	22.850	142.450	33	5.0	-1.76	0.37	6.96
NC	Fiji Islands	241	0521.12.1	-20.655	-177.765	379	5.4	0.00	-0.33	6.60
NC	Greenland Sea	244	0651.04.5	78.940	3.427	10	5.2	-11.31	0.23	-2.55
NC	Loyalty Islands	244	0822.29.6	-22.397	170.296	51	5.1	-7.32	0.50	11.77
NC	Mariana Islands	252	1430.20.2	12.834	143.906	33	5.1	-4.27	0.27	6.50
NC	Mariana Islands	252	15 6.31.1	12.649	144.109	33	5.0	-3.98	0.31	6.55
NC	Yukon, Canada	257	1025.02.2	61.550	-139.900	10	5.0	36.78	-0.17	-3.16
NC	Sierra Nevada, California	257	1900.00.0	37.226	-116.428	0	5.5	204.28	-1.13	-9.24
NC	Central California	260	2110.29.3	35.828	-121.323	9	5.2	45.18	-0.60	-7.42
NC	Kuril Islands	265	0632.37.6	49.619	156.590	33	5.5	53.42	-0.70	-2.06
NC	Unimak Island	267	2005.01.5	54.022	-164.223	33	5.0	-17.36	0.03	-2.61

* Not clustered.

satisfy the data. The residuals mostly contain information on the lateral variation, but for this quasi-horizontal structure they are ambiguous with respect to depth. We therefore constrain the model to be consistent with the results from deep seismic sounding, which then allows a unique, albeit smoothed, solution. Prior values for D and A (mean depth and velocity contrast) in equations (8) and (9) were taken from the results of deep seismic sounding [Puzyrev *et al.*, 1978], which finds a velocity reduction of about 5% just beneath the crust of the Baikal rift zone. According to surface wave analysis, this low-velocity layer extends from the Moho to the depth of more than 100 km [Zorin *et al.*, 1989]. Thus, as a starting model, we assume that the asthenosphere upwarp beneath our array extends from about 100 km at the side to the Moho at the center; a small value (0.3) for both σ_A and σ_D is used, thereby constraining both A and D .

For the inversion we used 638 travel times from 66 teleseismic events (Table 2) at 22 stations (Table 1) and a polynomial up to the 6th order ($n = 6$). Five of the 27 stations were not used in the inversion for one or more of the following reasons: (1) failure to record signals, (2) low signal-to-noise ratio, (3) obvious clock errors, and (4) too great a distance from other stations. The total number of parameters is 227 in a system of 638 equations augmented by 200 constraints (equations (5)-(9)). Parameters 1 through 66 are offset time (ΔT in equation (4)) for the 66 events; 67 through 132 and 133 through 198 are slopes (S_{xj} and S_{yj} in equation (4)) along the X and Y directions, respectively, for the events; 199 through 226 are polynomial coefficients (a_{lk} in equation (4)); and the 227th parameter is the velocity factor (A in equation (2)). Results of determination of ΔT_j , S_{xj} , and S_{yj} are shown in Table 2.

Depth to the interface beneath (X, Y) is then found by

$$H(X, Y) = A \times \left(\sum_{k=0}^n \sum_{l=0}^{n-k} a_{lk} X^k Y^l \right) \quad (10)$$

where a_{lk} are the polynomial coefficients found by the inversion.

Results

The square root of the unmodeled variance is 0.11 s, which is larger than the observational error range but is presumed to arise from oversimplification of the structure as a single undulating boundary separating two regions of constant but different velocity. The uncertainty in the depth of the boundary corresponding to the travel time misfit is ± 17 km. The results of the inversion are shown in Figures 4 and 5. The depth of the interface ranges from 93 km at 300 km west of the lake, beneath the craton, 34 km beneath the lake, and back to 49 km at 200 km east of the lake, beneath the fold belt (Figure 4). The upwarp is asymmetrical in terms of the difference between the slopes of the western and eastern flanks. The western edge is steeper. The asymmetrical shape is consistent with the results of gravity and magnetotelluric studies [Zorin, 1971; Popov, 1990]. The highest point of the lithosphere-asthenosphere boundary as constrained by DSS data, reaches 34 km near the east shore of the lake, in a region of hot springs (a favorite recreation spot during the field work).

The resultant velocity contrast factor (A) is 156 km/s. If we use deep seismic sounding results for the compressional wave velocity in the lithosphere immediately beneath the Moho as 8.1 km/s in the region away from

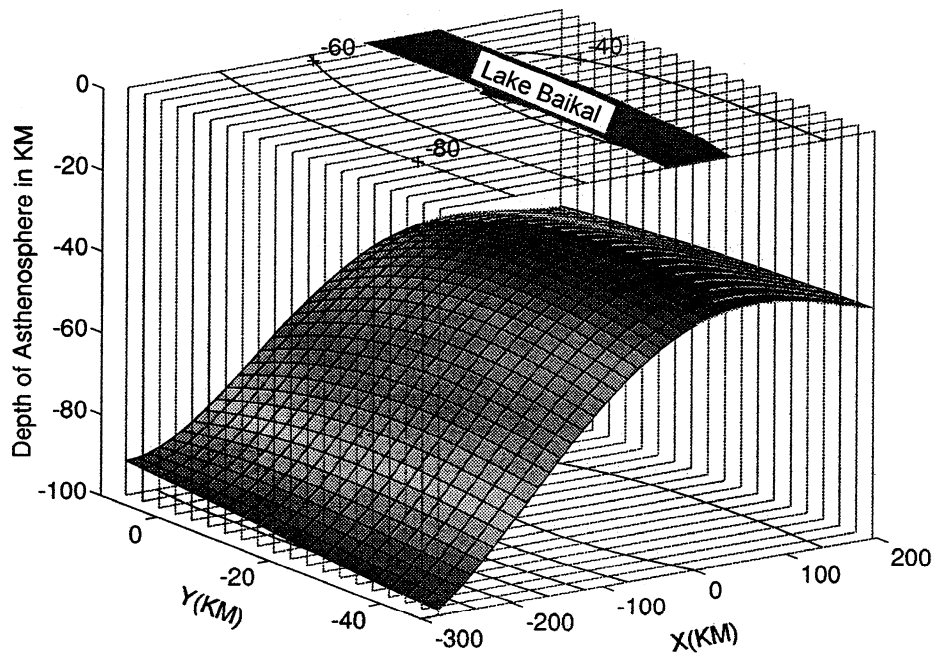


Figure 4. Polynomial surface determined by downward projection of the residual patterns of Figure 3. The X axis is taken along the line connecting the two stations at the end of the profile, and the Y axis is perpendicular to X and pointing to the northeast. The origin of the coordinate system is at the middle point of the lake, along the profile. The contours on the top and bottom planes are depth of the asthenosphere in kilometers. The shaded area on the top plane represents Lake Baikal. The uncertainty of the depth of the polynomial surface is ± 17 km.

the rift [Puzyrev *et al.*, 1978], we get an asthenospheric velocity of 7.7 km/s and the corresponding velocity contrast of -4.9% .

The result correlates well with gravity observations (Figure 5). The Bouguer gravity anomaly was separated into a short wavelength anomaly which we relate to shallow heterogeneity (surface to upper crust) and regional anomalies which are related to deep heterogeneity (Moho to 250 km) by using the decompenative forward-modeling method (developed by Zorin *et al.* [1989]; Cordell *et al.* [1991]). The residual mean squared difference between the regional anomaly and the calculated anomaly from our teleseismic model is 1.0 mGal. Density contrasts were adjusted in the calculation for a least-squares best fit resulting in values of -350 kg/m³ for the crust/mantle transition and 20 kg/m³ for the lithosphere-asthenosphere boundary. Using the crustal density (2790 kg/m³) proposed by Zorin [1977], the resultant densities are 3140 kg/m³ and 3120 kg/m³ for the lower lithosphere and upper asthenosphere, respectively. The initial crustal thickness used in the inversion was taken from the deep seismic sounding results and adjusted to improve the fit to the gravity data. The maximum adjustment was 2.5 km, which was felt to be within the errors of the deep seismic sounding data. The contrast of P wave velocity and density across the lithosphere-asthenosphere boundary is -4.9% and -0.6% , respectively. This combination of large velocity contrast and small density contrast may indicate a small fraction of partial melt within the upwarded asthenosphere [Davis *et al.*, 1984; Davis, 1991].

Relative t^* (travel time divided by Q) values along the profile supports this view. The intrinsic attenuation of a medium, Q is defined as [Knopoff, 1964]

$$\frac{2\pi}{Q} = -\frac{\Delta E}{E} \quad (11)$$

where E is the maximum elastic energy within a given volume and ΔE is loss of energy per cycle of harmonic motion. Writing (11) in differential form for a monochromatic wave of period τ [Stacey, 1992]

$$\frac{1}{E} \frac{dE}{dt} = -\frac{2\pi}{Q\tau} \quad (12)$$

and integrating by taking into the relation between energy E and amplitude A , that is, $E \propto A^2$

$$A = A_0 \exp\left(-\frac{\pi}{Q\tau} t\right) = A_0 \exp\left(-\frac{\pi}{\tau} t^*\right) \quad (13)$$

where t is the travel time. The relative t^* between two stations is calculated from a usual spectrum ratio routine through

$$\frac{A_2}{A_1} = \exp\left(-\frac{\pi}{\tau}(t^*_2 - t^*_1)\right). \quad (14)$$

The t^* values relative to station 01 based on the 13 events most suitable for this analysis are calculated by using the first 10 s after the first P wave. The events used in t^* calculations are those that have a high signal-to-noise ratio, lie approximately on the great circle of

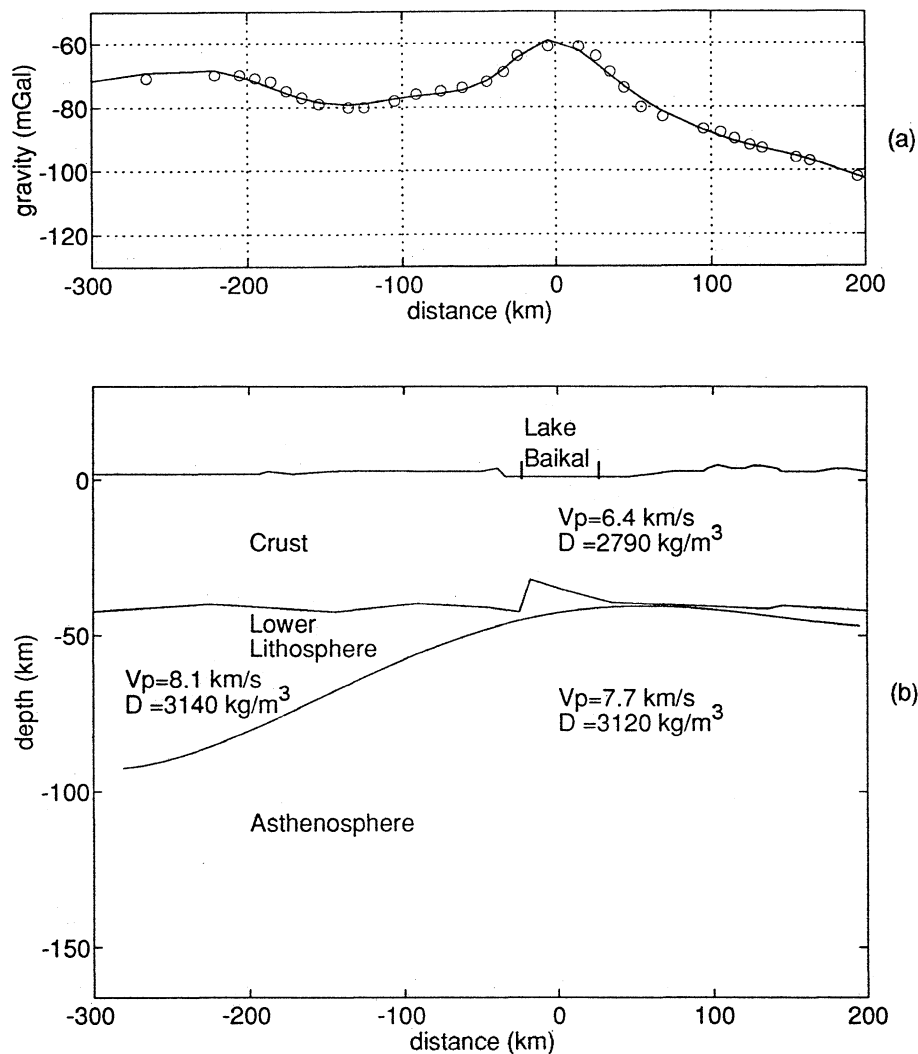


Figure 5. Regional Bouguer gravity anomaly and cross section of Figure 4 along the profile. Crustal thicknesses are taken from deep seismic sounding. The averaged misfit between the calculated gravity anomaly (solid line in Figure 5a) from our deep structure (Figure 5b) and measured regional anomaly (circles in Figure 5a) is about 1.0 mGal. The best fitting asthenosphere/lithosphere density contrast is -0.6%. The shape of the Moho causes the short-wavelength variation of the gravity field while that of the lithosphere-asthenosphere boundary contributes most of the long-wavelength variation of the field, that is, the decreasing trend toward the east. The vertical axis is exaggerated by 2 times in Figure 5b.

the profile, originate between 30° and 75° , and are recorded by enough stations with good readings [Halderman and Davis, 1991]. The resulting relative t^* values increase eastward with a peak to peak difference of 0.1 seconds and at the rift region a 0.06-s local anomaly is observed (Figure 6).

We used a method developed by Halderman and Davis [1991] to estimate the Q value of the asthenosphere. We calculated the slope, α , of the relative t^* versus relative travel time residuals plot (Figure 7), which we find to be 0.0565 ± 0.0221 . The quality factor of the lithosphere is determined by

$$Q_2 = \frac{V_1 Q_1}{\alpha Q_1 (V_1 - V_2) + V_2} \quad (15)$$

where V_1 , V_2 and Q_1 , Q_2 are the velocities and quality

factors of the lithosphere and the asthenosphere, respectively. If we assume that the Q in the lithosphere is 200 and use the velocities found by the inversion above, we get a Q value for the asthenosphere of 132 ± 20 .

Conclusion and Comparison With Other Rifts

Comparison of the gravity and topography across the world's major continental rift zones [Davis et al., 1993] shows that the heights of regional uplift and the magnitudes of regional Bouguer anomalies gradually decrease in the following series: East African, Rio Grande, Baikal, and Rhine graben. A similar pattern is seen in the teleseismically determined mantle anomalies. The regional travel time anomaly at Lake Baikal of 1.1 s

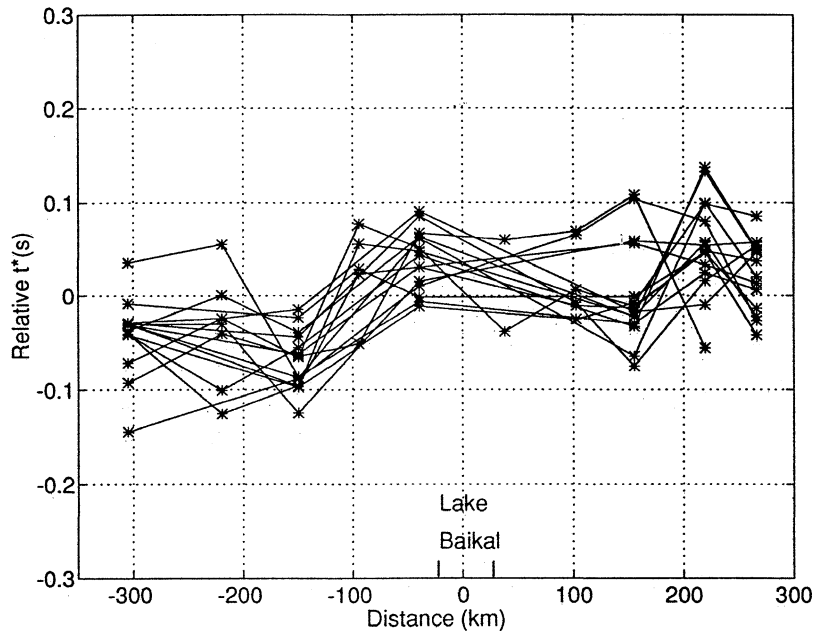


Figure 6. Spatial distribution of t^* along the profile estimated from 13 events along the profile. Note the greater attenuation beneath Lake Baikal. Zero on the horizontal coordinate corresponds to the center of the lake.

is significantly greater than the 0.2 s observed on the Rhine graben [Glahn and Granet, 1992] but less than the 1.5 s of the Rio Grande experiments [Davis *et al.*, 1984; Parker *et al.*, 1984] and the 2.0 s seen in East Africa [Savage and Long, 1985; Dahlheim *et al.*, 1989; Davis, 1991]. The same pattern also emerges in the Q studies. For a lithospheric Q of 200 the asthenospheric Q beneath the East African rift was found to be 32, while that beneath the Rio Grande was 109 [Halderman and Davis, 1991], and our value found above for

the Baikal rift is 132. (Q for the Rhine graben has not been determined). If low velocities and high attenuation are associated with low density, these results suggest that the isostatic compensation of the uplift zone about Lake Baikal lies in the mantle.

Beneath both the Rio Grande [Spence and Gross, 1990; Davis *et al.*, 1984; Davis *et al.*, 1993] and Baikal rifts, the axis of mantle anomalies are not situated just beneath, or aligned with, the surface grabens; whereas for the East African rift they are [Dahlheim *et al.*, 1989;

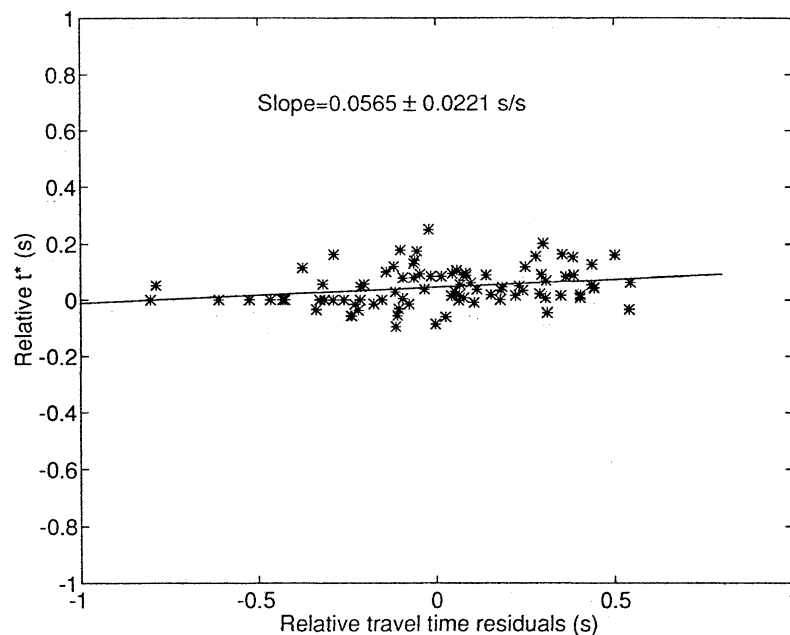


Figure 7. A plot of relative t^* versus relative travel time residuals.

Green et al., 1991]. For the Rio Grande, the mantle anomaly trends northeast, that is, at about 45° to the strike of the rift. For the Rhine graben the mantle anomalies are very small, suggesting that mantle effects are less important in generating rifting there than the plate collision forces that have given rise to the Alps. In contrast to the African plate, both the North American and Eurasian plates are in motion relative to the hotspot reference frame. Thus if vertical mantle flow is important at the initiation of continental rifting in these cases, the present configuration, some 30 million years later, is not unexpectedly displaced from the surface grabens.

Acknowledgments. Field work in Russia was supported by the Russian Academy of Sciences. UCLA and University of Wisconsin, Madison, were supported by DARPA award F2901-91-K-DB17. The 11 sets of Reftek recorders and 5 L4C seismometers were provided by the PASSCAL Instrument center at Lamont-Doherty Earth Observatory. We wish to express our gratitude to the following people who helped in the field work: R. Abernathy, O. Artyomov, A. Baduev, R. Busby, C. Davis, L. Delitsin, W. Green, M. Karpachov, V. Kozhevnikov, O. Masalsky, V. Mordvinova, S. Panasyuk, T. Perepelova, L. Powell, V. Tairov, and W. Unger.

References

- Cordell, L., Yu. A. Zorin, and G. R. Keller, The decompensative gravity anomaly and deep structure of the region of the Rio Grande rift, *J. Geophys. Res.*, **96**, 6557-6568, 1991.
- Dahlheim, H.-A., P. M. Davis, and U. Achauer, Teleseismic investigation of the East African Rift-Kenya, *J. Afr. Earth Sci.*, **8**(2-4), 461-470, 1989.
- Davis, P. M., Continental rift structures and dynamics with reference to teleseismic studies of the Rio Grande and East African rifts, *Tectonophysics*, **197**, 309-325, 1991.
- Davis, P. M., E. C. Parker, J. R. Evans, H. M. Iyer, and K. H. Olsen, Teleseismic deep sounding of the velocity structure beneath the Rio Grande rift, *Field Conf. Guideb.*, *N. M. Geol. Soc.*, **35**, 29-38, 1984.
- Davis, P. M., P. Slack, H.-A. Dahlheim, W. V. Green, R. P. Meyer, U. Achauer, A. Glahn, and M. Granet, Teleseismic tomography of continental rift zones, in *Seismic Tomography: Theory and Practice*, edited by H. M. Iyer and H. Hirata, pp. 397-439, Chapman and Hall, London, 1993.
- Doser, D. I., Faulting within the western Baikal rift as characterized by earthquake studies, *Tectonophysics*, **196**, 87-107, 1991.
- Dziewonski, A. M., and D. L. Anderson, Preliminary reference Earth model, *Phys. Earth Planet. Inter.*, **25**, 297-356, 1981.
- Glahn, A., and M. Granet, 3-D structure of the lithosphere beneath the southern Rhine Graben area, *Tectonophysics*, **208**, 149-158, 1992.
- Golenetsky, S. I., Problems of the seismicity of the Baikal rift zone, *J. Geodynamics*, **11**, 293-307, 1990.
- Golenetsky, S. I., and L. A. Misharina, Seismicity and earthquake focal mechanisms in the Baikal rift zone, *Tectonophysics*, **45**, 71-85, 1978.
- Gornostaiev, V. P., V. I. Michailovskiy, and V. J. Pospelov, Deep magnetotelluric soundings on the south of the Siberian platform in the Baikal rift zone, *Geol. Geofiz.*, **4**, 111-118, 1970.
- Green, W. V., U. Achauer, and R. P. Meyer, A three dimensional image of the crust and upper mantle beneath the Kenya rift, *Nature*, **354**, 199-203, 1991.
- Halderman, T. P., and P. M. Davis, Q_p beneath the Rio Grande and east African rift zones, *J. Geophys. Res.*, **96**, 10,113-10,128, 1991.
- Jackson, D. D., and M. Matsu'ura, A Bayesian approach to nonlinear inversion, *J. Geophys. Res.*, **90**, 581-591, 1985.
- Kennett, B. L. N., and E. R. Engdahl, Travel times for global earthquake location and phase identification, *Geophys. J. Int.*, **105**, 429-465, 1991.
- Knopoff, L., *Q*, *Rev. Geophys.*, **2**, 625-660, 1964.
- Logatchev, N. A., and N. A. Florensov, The Baikal system of rift valleys, *Tectonophysics*, **45**, 1-13, 1978.
- Logatchev, N. A., and Y. A. Zorin, Evidence and causes of the two-stage development of the Baikal rift, *Tectonophysics*, **143**, 225-234, 1987.
- Lubimova, E. A., Heat flow patterns in Baikal and other rift zones, *Tectonophysics*, **8**, 457-467, 1969.
- Lysak, S. V., Terrestrial heat flow in the south of east Siberia, *Tectonophysics*, **103**, 205-215, 1984.
- Morgan, P., Heat flow in rift zones, in *Continental and Oceanic Rifts, Geodyn. Ser.*, vol. 8, edited by G. Palmason, pp. 107-122, AGU, Washington, D.C., 1982.
- Parker, E. C., P. M. Davis, J. R. Evans, H. M. Iyer, and K. H. Olsen, Upwarp of anomalous asthenosphere beneath the Rio Grande rift, *Nature*, **312**, 354-356, 1984.
- Popov, A. M., A deep geophysical study in the Baikal region, *Pure Appl. Geophys.*, **134**, 575-587, 1990.
- Puzyrev, N. N., M. M. Mandelbaum, S. V. Krylov, B. P. Mishenkin, G. V. Petrik, and G. V. Krupskaya, Deep structure of the Baikal and other continental rift zones from seismic data, *Tectonophysics*, **45**, 15-22, 1978.
- Savage, J. E. G., and R. E. Long, Lithospheric structure beneath the Kenya Dome, *Geophys. J. R. Astron. Soc.*, **82**, 461-477, 1985.
- Spence, W., and R. S. Gross, A tomographic glimpse of the upper mantle source of magmas of the Jemez lineament, New Mexico, *J. Geophys. Res.*, **98**, 10,829-10,849, 1990.
- Stacey, F., *Physics of the Earth*, Brookfield, Brisbane, Australia, 1992.
- Zamarayev, S. M., and V. V. Ruzhich, On relationships between the Baikal rift zone and ancient structures, *Tectonophysics*, **45**, 41-47, 1978.
- Zorin, Y. A., *Recent Structure and Isostasy of the Baikal Rift Zone and Adjacent Territories*, (in Russian), 168 pp., Nauka, Moscow, 1971.
- Zorin, Y. A., Isostasy and gravimetric model of the Earth's crust and upper mantle. in *Essays on Deep Structure of the Baikal rift*, (in Russian), edited by N. A. Florensov, pp. 83-98, Nauka, Novosibirsk, 1977.
- Zorin, Y. A., and L. Cordell, Crustal extension in the Baikal rift zone, *Tectonophysics*, **198**, 117-121, 1991.
- Zorin, Y. A., V. M. Kozhevnikov, M. R. Novoselova, and E. K. Turutanov, Thickness of the lithosphere beneath the Baikal rift zone and adjacent regions, *Tectonophysics*, **168**, 327-337, 1989.

P.D. Burkholder and R.P. Meyer, Department of Geology and Geophysics, University of Wisconsin, 1215 West Dayton Street, Madison, WI 53706.

S. Gao, P.M. Davis, H. Liu, and P.D. Slack, Department of Earth and Space Sciences, University of California, 405 Hilgard Avenue, Los Angeles, CA 90024-1567.

M. Kogan, Institute of Physics of the Earth, Russian Academy of Sciences, Moscow, Russia.

N.A. Logatchev and Y.A. Zorin, Institute of the Earth's Crust, Siberian Branch of the Russian Academy of Sciences, Irkutsk, Russia.

(Received April 21, 1993; revised March 15, 1994; accepted March 21, 1994.)